

Charge disproportionation and collinear magnetic order in the frustrated triangular antiferromagnet AgNiO_2

E. Wawrzyńska,¹ R. Coldea,¹ E. M. Wheeler,^{2,3} T. Sörgel,⁴ M. Jansen,⁴ R. M. Ibberson,⁵ P. G. Radaelli,^{5,6} and M. M. Koza³

¹*H. H. Wills Physics Laboratory, University of Bristol, Tyndall Avenue, Bristol BS8 1TL, United Kingdom*

²*Clarendon Laboratory, University of Oxford, Parks Road, Oxford OX1 3PU, United Kingdom*

³*Institut Laue-Langevin, B \hat{o} ite Postale 156, 38042 Grenoble Cedex 9, France*

⁴*Max-Planck Institut für Festkörperforschung, Heisenbergstrasse 1, D-70569 Stuttgart, Germany*

⁵*ISIS Facility, Rutherford Appleton Laboratory, Chilton, Didcot OX11 0QX, United Kingdom*

⁶*Department of Physics and Astronomy, University College London, Gower Street, London WC1E 6BT, United Kingdom*

(Received 5 October 2007; revised manuscript received 29 January 2008; published 28 March 2008)

We report a high-resolution neutron diffraction study of the crystal and magnetic structure of the orbitally degenerate frustrated metallic magnet AgNiO_2 . At high temperatures the structure is hexagonal with a single crystallographic Ni site, low-spin Ni^{3+} with spin 1/2 and twofold orbital degeneracy, arranged in an antiferromagnetic triangular lattice with frustrated spin and orbital order. A structural transition occurs upon cooling below 365 K to a tripled hexagonal unit cell containing three crystallographically distinct Ni sites with expanded and contracted NiO_6 octahedra, naturally explained by spontaneous charge order on the Ni triangular layers. No Jahn-Teller distortions occur, suggesting that charge order occurs in order to lift the orbital degeneracy. Symmetry analysis of the inferred Ni charge order pattern and the observed oxygen displacement pattern suggests that the transition could be mediated by charge fluctuations at the Ni sites coupled to a soft oxygen optical phonon breathing mode. At low temperatures the electron-rich Ni sublattice (assigned to a valence close to Ni^{2+} with $S=1$) orders magnetically into a collinear stripe structure of ferromagnetic rows ordered antiferromagnetically in the triangular planes. We discuss the stability of this uncommon spin order pattern in the context of an easy-axis triangular antiferromagnet with additional weak second-neighbor interactions and interlayer couplings.

DOI: [10.1103/PhysRevB.77.094439](https://doi.org/10.1103/PhysRevB.77.094439)

PACS number(s): 75.25.+z, 71.45.Lr, 75.10.Jm, 75.40.Cx

I. INTRODUCTION

Two-dimensional frustrated quantum magnets have attracted a wide interest theoretically¹ and experimentally² as possible candidates to display strong fluctuations that could potentially stabilize unconventional ordered phases,³ spin-liquid⁴ or orbital-liquid⁵ states. Low-spin triangular-lattice antiferromagnets are canonical frustrated models and the delafossite AgNiO_2 with Ni ions arranged in well-separated triangular lattices has been proposed to show frustration effects both in the magnetic as well as in the orbital sector. Based on magnetic susceptibility measurements, Shin *et al.*⁶ proposed that Ni ions are in the low-spin configuration Ni^{3+} ($t_{2g}^6 e_g^1$) with $S=1/2$, coupled by dominant in-plane frustrated antiferromagnetic interactions, and from x-ray measurements they proposed a high-symmetry crystal structure where each Ni ion has an unpaired electron in a doubly degenerate e_g orbital. The cooperative orbital order is strongly frustrated because the orbital interactions have a strong bond-directional dependence⁷ favoring different orbitals for pairs of Ni ions along the three different directions in the triangular lattice, and this leads to a large manifold of degenerate mean-field states. The ground state in this spin-orbital problem is still highly debated theoretically with proposals ranging from orbital liquids to nontrivial forms of orbital order depending on fine details of the interactions.^{3,5,8} Among the experimentally explored candidate spin-1/2 materials to display this physics are NaTiO_2 (nonmagnetic after structural transition at low temperatures),⁹ NaNiO_2 [a quasi-two-dimensional (2D) spin-1/2 ferromagnet with ferrodistor-

tive orbital order],¹⁰ and LiNiO_2 (no long-range magnetic or orbital order, but evidence for local Jahn-Teller distortions, difficulty in preparing pure stoichiometric samples).⁸ The triangular magnet AgNiO_2 and the two-silver-layer version Ag_2NiO_2 (Refs. 11 and 12) are relatively unexplored experimentally and promise to be rather different from the above-mentioned systems, as they both show dominant *antiferromagnetic* interactions,¹³ thus potentially displaying frustrated magnetism.

AgNiO_2 is part of the large family of delafossite $A^+M^{3+}\text{O}_2$ materials often studied as candidate two-dimensional frustrated magnets because the transition metal ion (M) sits at the vertices of a triangular lattice in the basal plane, made up of a network of edge-sharing MO_6 octahedra. Like most delafossites, it occurs in two structural polytypes which differ in the way the NiO_2 layers are stacked along the c axis: a three-stage structure, where successive layers are in the same orientation but have an in-plane offset with Ni ions forming a three-stage staircase along the c axis ($3R$ polytype, rhombohedral space group $R\bar{3}m$; Refs. 6 and 14), or a two-stage structure, where successive layers are stacked right on top of each other but are rotated by 180° [$2H$ polytype, hexagonal space group $P6_3/mmc$ shown in Fig. 1(a); Ref. 15]. All measurements reported here have been made on the less-studied two-stage polytype, the so called $2H\text{-AgNiO}_2$, recently synthesized using high-oxygen-pressure techniques.¹⁵ This polytype has metalliclike conductivity from 300 K down to low temperatures and the susceptibility indicates antiferromagnetic order near 20 K,¹⁵ but the magnetic structure has not been determined up to now.

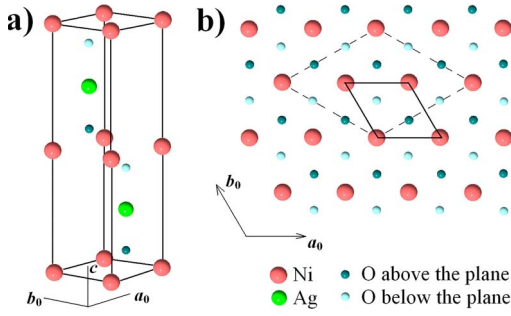


FIG. 1. (Color online) Nominal crystal structure of $2H\text{-AgNiO}_2$ deduced from x-ray measurements in Ref. 15 (space group $P6_3/mmc$, D_{6h}^4). (a) There are two NiO_2 layers per unit cell related by a mirror plane reflection through the Ag^+ layer at $z=1/4$. (b) Basal plane showing the triangular network of Ni ions (large red balls) coordinated by oxygens (small blue balls). The thick solid line contour shows the unit cell and the dashed line shows the unit cell tripling in the distorted structure.

In the ideal crystal structure of both $3R$ and $2H$ polytypes of AgNiO_2 Ni ions have both spin and orbital degrees of freedom. The local crystal field is octahedral and near cubic and in the case of the strong crystal field proposed herein^{6,15} the electronic state of Ni^{3+} ($3d^7$) is the low-spin state $t_{2g}^6 e_g^1$ with one unpaired electron (spin $1/2$) in the upper e_g level. A small trigonal distortion present in the crystal structure due to squashing of the NiO_6 octahedra along the c axis changes the detailed wave functions of the orbital states but does not lift the twofold degeneracy of the upper e_g level because it preserves a local threefold symmetry rotation axis along c . Each Ni ion has a tendency to locally distort the environment to lower its orbital energy due to the Jahn-Teller effect; however, the cooperative orbital order on the triangular lattice is frustrated as the orbital exchange favors occupation of different orbitals for pairs of Ni ions along the three different in-plane directions. Such systems are susceptible to forming an orbital-liquid state at low temperatures or to having the orbital degeneracy lifted by structural distortions.

In measurements reported here, we find evidence for a weak structural modulation in $2H\text{-AgNiO}_2$, leading to a tripling of the unit cell in the hexagonal basal plane. This can be naturally explained by charge disproportionation on the Ni sites into three sublattices, which we propose occurs in order to lift the orbital degeneracy of the Ni^{3+} ions. This physics is in sharp contrast to the insulator NaNiO_2 where the orbital degeneracy is lifted by Jahn-Teller orbital order, leading to a monoclinic crystal structure.¹⁰ We attribute this difference to the fact that, because $2H\text{-AgNiO}_2$ is metallic, charge transfer can be an energetically more favorable mechanism to lift the orbital degeneracy compared to local Jahn-Teller distortions found in more localized systems.

At low temperatures the electron-rich Ni sublattice (attributed to a valence close to Ni^{2+} with spin $S=1$) orders magnetically in a collinear stripe structure with spins pointing along the c axis and arranged in alternating ferromagnetic rows in the triangular plane. This magnetic structure cannot be explained at the mean-field level by a minimal spin model on a triangular lattice containing only nearest-neighbor anti-

ferromagnetic exchange and easy-axis anisotropy, and we propose that it is stabilized by additional weak second-neighbor antiferromagnetic in-plane interactions and/or weak ferromagnetic interlayer couplings.

The rest of the paper is organized as follows. Section II presents the experimental details of the neutron, x-ray, susceptibility, and specific heat measurements. Diffraction measurements of the room-temperature crystal structure are presented and analyzed in Sec. III, where a lower-symmetry space group is proposed to accommodate the observed structural modulation. A transition to the high-symmetry, undistorted crystal structure is observed upon heating to high temperatures, and this is discussed in Sec. IV, followed by a symmetry analysis of the structural distortion in terms of symmetry-allowed basis vectors in Sec. V. This is used to propose that the mechanism for the structural distortion is charge fluctuations at the Ni site coupled with a soft zone-boundary optical phonon involving oxygen breathing modes (further calculations using corepresentation symmetry analysis to uniquely determine the distorted space group are presented in Appendix B). Susceptibility and specific heat measurements are shown in Sec. VI, followed by measurements of the magnetic structure analyzed in terms of symmetry-allowed basis vectors and discussed in terms of a minimal Hamiltonian containing exchange and easy-axis anisotropy (Sec. VII). Finally, the results are summarized and discussed in Sec. VIII. For completeness we include in Appendix A a list of the measured supercell and magnetic structure factors. A partial account of the results describing the room-temperature crystal structure and low-temperature magnetic order has been reported in Ref. 16.

II. EXPERIMENTAL DETAILS

Powder samples of $2H\text{-AgNiO}_2$ (<1% admixture of the $3R$ polytype) were prepared from Ag_2O and $\text{Ni}(\text{OH})_2$ using high oxygen pressures (130 MPa) as described in Ref. 15. Neutron diffraction patterns to probe the crystal and magnetic structure were collected using the high-resolution backscattering time-of-flight diffractometers OSIRIS ($0.65 < Q < 6 \text{ \AA}^{-1}$) and HRPD ($2 < Q < 9 \text{ \AA}^{-1}$) at the ISIS Facility of the Rutherford Appleton Laboratory in the United Kingdom. Preliminary measurements were also performed using GEM at ISIS and the monochromatic neutron diffractometer D1B at the Institute Laue-Langevin in France. The magnetic order parameter was obtained from elastic neutron scattering measurements using the direct-geometry time-of-flight spectrometer IN6 and the temperature dependence of the lattice constants was also measured on D2B, both at the ILL. X-ray powder diffraction measurements to help solve the crystal structure at room temperature were made using a Philips X'pert diffractometer ($\lambda_{\text{Cu } K\alpha} = 1.54 \text{ \AA}$). Structural and magnetic refinement was made using the FULLPROF program.¹⁷ Susceptibility measurements were made using a superconducting quantum interference device (SQUID) magnetometer (Quantum Design MPMS) and specific heat data were collected on a pressed powder pellet using a Quantum Design physical properties measurement system.

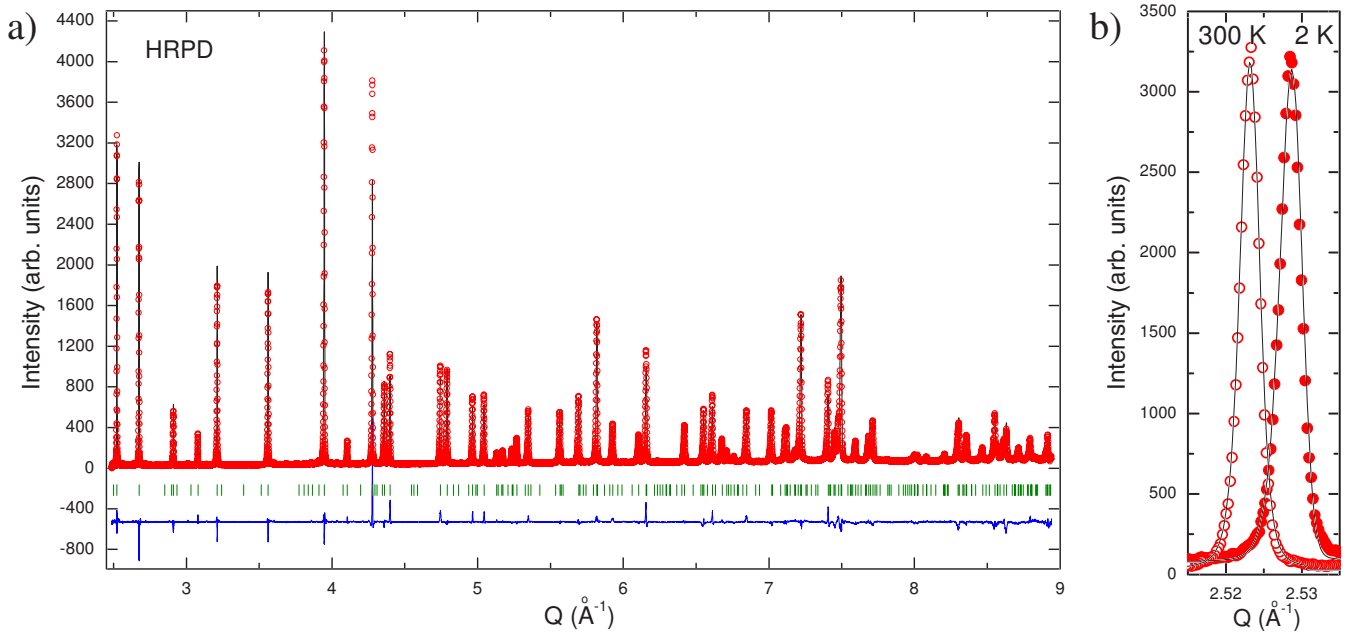


FIG. 2. (Color online) (a) Room temperature (300 K) neutron diffraction pattern obtained using HRPD (resolution $\Delta Q/Q \sim 10^{-3}$, 15 h counting on an 11 g powder sample). The solid curve through the data points is a fit to the distorted $P6_322$ space group. Vertical bars indicate Bragg peak positions and the bottom curve shows the difference between the fit and the data. Zoomed-in regions showing weak supercell peaks are plotted in Fig. 3. (b) Detail of the (111) peak line shape expected to split in the case of a structural distortion to an orthorhombic or monoclinic structure. No splitting could be detected, and the line shape at both 300 (open symbols) and 2 K (filled circles) could be well described by a resolution-convolved profile for the hexagonal $P6_322$ space group (solid lines) with lattice parameters adjusted for thermal contraction upon cooling.

III. CRYSTAL STRUCTURE

The neutron powder diffraction pattern collected at room temperature ($T=300$ K, Fig. 2) is overall in good agreement with the hexagonal space group $P6_3/mmc$ proposed before.¹⁵ However, a close inspection shows the presence of a number of additional low-intensity peaks (below 1% of the main peak) that could be indexed in this space group by *fractional* wave vectors such as $(2/3, -1/3, 0)$ and $(2/3, -1/3, 1)$ in Fig. 3(b), and such supercell peaks systematically accompany the main structural peaks throughout the wide Q range probed [see Fig. 3(a)] and are displaced in Q following the lattice contraction upon cooling [see the paired up-down Figs 3(b) and 3(c), 3(e) and 3(f), and 3(h) and 3(i)]. These extra peaks are naturally interpreted in terms of a structural modulation equivalent to a tripling of the unit cell in the basal plane. Complementary x-ray measurements [Figs. 3(d), 3(g), and 3(j)] did not show a measurable intensity at the supercell positions, suggesting that the structural modulation involves mainly displacements of the light oxygen ions, which have a very small x-ray cross section, as any significant displacements of the heavier Ag or Ni ions would have implied occurrence of supercell peaks not observed in the collected x-ray pattern. Therefore to model the distortion we refined only the oxygen positions and considered in order of decreasing symmetry all subgroups of the ideal structure ($P6_3/mmc$) compatible with a tripling of the unit cell in the ab plane, i.e., a unit cell of size $\sqrt{3}a_0 \times \sqrt{3}a_0 \times c$ (six Ag, six Ni, and twelve O atoms per unit cell). We eliminated the space groups that were not compatible with the observed

low-temperature magnetic structure (see Sec. VII) where two Ni ions in the unit cell are magnetically ordered and four are unordered, i.e., we considered only the space groups where the magnetically ordered and unordered Ni ions occupied distinct crystallographic sites. The highest-symmetry subgroup in which both the structural and magnetic data could be described is $P6_322$ (no. 182) where all 12 oxygen atoms are symmetry related and compared to the ideal structure are displaced by a small amount ϵ along one of the in-plane triangular directions. The observed supercell reflections could be well described by this model, and the best fit to the data is shown in Figs. 2 and 3 (solid lines, $R_{\text{Bragg}}=5.55\%$, $R_{\text{F}}=6.49\%$) (structure factors are listed in Table V in Appendix A). The obtained lattice parameters and positions in the unit cell are listed in Table I. As a further test we refined the lattice parameters using only the main peaks or only the supercell peaks and obtained similar values [$a=5.09082(1)$ Å, $c=12.24984(4)$ Å and $a=5.0908(2)$ Å, $c=12.250(2)$ Å, respectively], corroborating the fact that the weak supercell peaks belong to the same phase as the main peaks and are not due to an extra phase.

Figure 4 shows a schematic diagram of the $z=1/4$ NiO_2 layer of the distorted structure. The distortion preserves the threefold rotation axis at each Ni site but the displacements of the oxygens lead to one Ni site with expanded Ni-O bonds (Ni1) and two other sites with contracted bonds (Ni2 and Ni3); the black circles centered on the Ni sites correspond to Ni-O distances of 2.022 Å (Ni1) and 1.934 Å (Ni2 and Ni3), respectively. In Ni^{2+} oxides¹⁸ typical Ni-O bond distances are about ~ 2.09 Å, whereas in Ni^{4+} oxides¹⁹ they

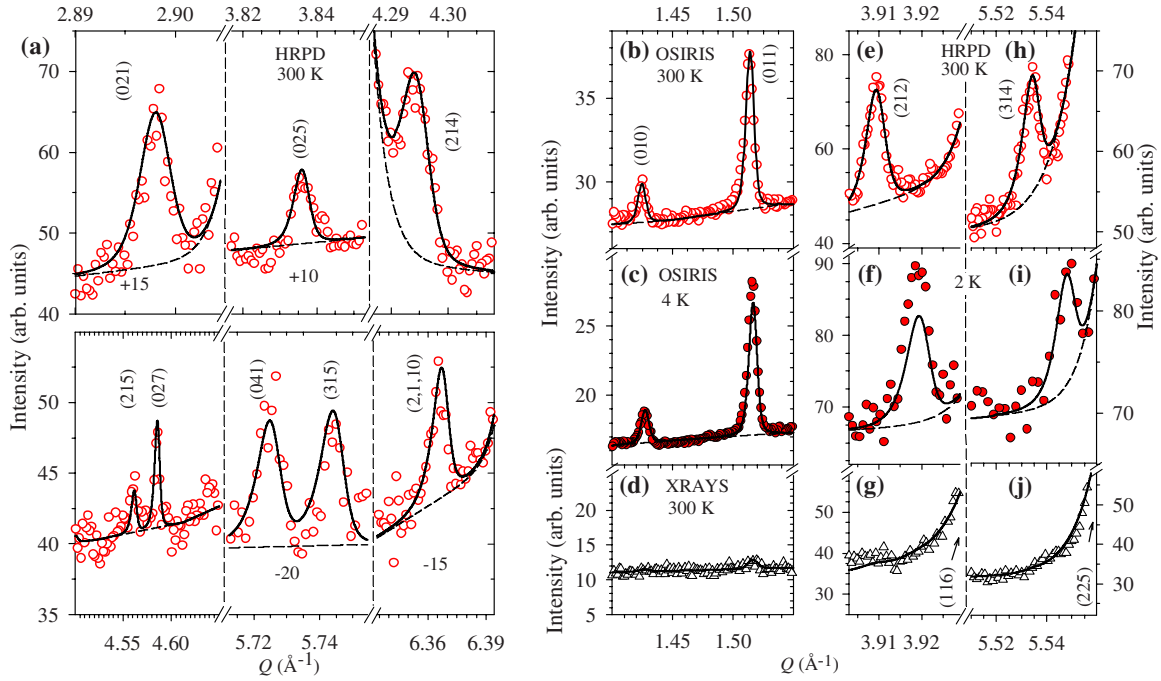


FIG. 3. (Color online) Zoomed-in regions of the 300 K neutron diffraction pattern (a), (b), (e), and (h) showing a number of the weak supercell reflections disallowed in the ideal $P6_3/mmc$ structure and associated with a tripling of the unit cell in the ab plane. Solid lines are the calculated profile for the distorted $P6_322$ structure in Fig. 4 and dashed lines show the estimated local background including the resolution tails of nearby main structural peaks (data in some panels are shifted vertically by indicated amounts for clarity). Paired panels (b),(c), (e),(f), and (h),(i) show how the supercell peaks are displaced in Q following the lattice contraction upon cooling (the base temperature data have a higher overall background as they were collected in a cryostat). Supercell peaks are not observed in the x-ray data in (d), (g), and (j), consistent with the structural modulation involving mainly displacements of the light oxygen ions.

decrease to 1.92 Å. This comparison suggests a charge disproportionation among the Ni sites on the triangular layers in $2H$ - AgNiO_2 between electron-rich Ni1 sites (expanded NiO_6 octahedron) with valence close to Ni^{2+} and electron-depleted sites Ni2 and Ni3 (contracted octahedra) close to $\text{Ni}^{3.5+}$ (to ensure charge neutrality). Using a phenomenological bond-valence model²⁰ to relate the valence of the central ion to the bond lengths, $v = \sum_i e^{(r_0 - r_i)/B}$ where $B = 0.37$ Å and $r_0 = 1.686$ Å for the Ni^{3+} - O^{2-} pair, gives nominal valences in the ionic limit for the three sites as 2.42 (Ni1) and 3.07 (Ni2

and Ni3), suggesting a significant, but most likely only partial, charge disproportionation. We note that the bond lengths found in $2H$ - AgNiO_2 are similar to those found in YNiO_3 [$d(\text{Ni1-O}) = 1.923$ Å and $d(\text{Ni2-O}) = 1.994$ Å; Ref. 21], proposed to have a charge disproportionation into two Ni sublattices of valences $\text{Ni}^{3 \pm \sigma}$ ($\sigma \approx 0.35$).

Upon cooling to lower temperatures no evidence for a further structural distortion could be found. At 2 K the main and supercell peaks are displaced in wave vector following the lattice contraction and the structural peaks could be well

TABLE I. Lattice parameters and atomic positions in the unit cell in the ideal ($P6_3/mmc$) and the distorted ($P6_322$) structural space groups at 300 K. Oxygen positions are parametrized by an out-of-plane height $z_0 = 0.080\ 50(5)$ and an in-plane displacement $\epsilon = 0.0133(2)$. The distorted unit cell is tripled in the hexagonal plane with an unchanged extent along the c axis, but the origin is shifted by $c/4$ such that the two NiO_2 layers appear now at $z = 1/4$ and $3/4$. Throughout this paper we use different symbols a_0 and $a = \sqrt{3}a_0$ to denote the hexagonal lattice parameter of the ideal and distorted structures, respectively.

$P6_3/mmc$ (no. 194)			$P6_322$ (no. 182)		
	$a_0 = 2.939\ 19(5)$ Å			$a = 5.090\ 8(1)$ Å	
	$c = 12.249\ 8(1)$ Å			$c = 12.249\ 8(1)$ Å	
Atom	Site	(x, y, z)	Atom	Site	(x, y, z)
Ni	$2a$	(0,0,0)	Ni1	$2c$	($1/3, 2/3, 1/4$)
			Ni2	$2b$	(0,0, $1/4$)
			Ni3	$2d$	($1/3, 2/3, 3/4$)
Ag	$2c$	($2/3, 1/3, 1/4$)	Ag	$6g$	($2/3, 0, 0$)
O	$4f$	($2/3, 1/3, z_0$)	O	$12i$	($1/3, \epsilon, 1/4 + z_0$)

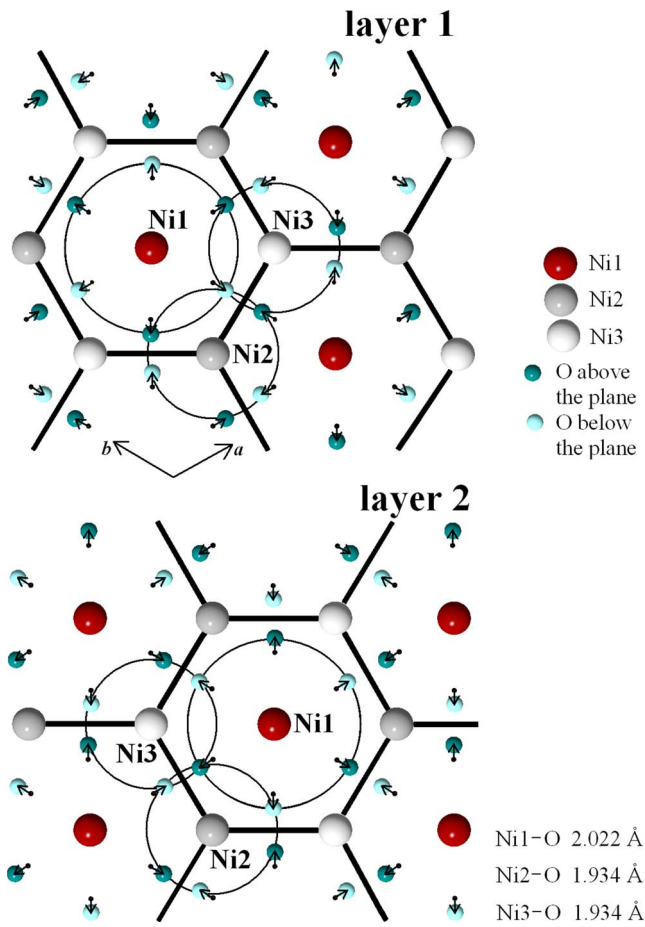


FIG. 4. (Color online) (Top) Schematic diagram of the NiO_2 layer at $z=1/4$ showing how the displacements (small arrows) of the oxygen ions (small balls) lead to a periodic arrangement of expanded (large circle, Ni1) and contracted (small circles, Ni2,3) NiO_6 octahedra. Thick hexagonal contour shows the honeycomb network of contracted sites. The origin of the coordinate system is at the circled Ni2 site. (Bottom) The expanded site Ni1 has a staggered zigzag arrangement between even and odd layers stacked along the c axis. Layer 2 in the unit cell ($z=3/4$ and $-1/4$) is obtained from layer 1 by 180° rotation around the central $(1/2, 1/2, z)$ axis followed by a $c/2$ translation.

described [see solid lines in Figs. 3(c), 3(f), and 3(i)] by the same crystal structure as at 300 K but with shorter lattice parameters $a=5.081\,10(2)$ Å and $c=12.246\,70(7)$ Å ($R_{\text{Bragg}}=4.45\%$, $R_{\text{F}}=5.53\%$). We note that the related triangular-lattice material NaNiO_2 behaves very differently, showing a strong ferrodistorive transition into a low-temperature monoclinic structure with a significant difference (4%) in the two in-plane lattice parameters.¹⁰ We tested for such a scenario in $2H\text{-AgNiO}_2$, where a departure from hexagonal symmetry could be accommodated within the orthorhombic $Cmcm$ space group with lattice parameters $\tilde{a} \times \tilde{b} \times c$. Within the experimental accuracy no splitting of the main peaks could be detected [see Fig. 2(b)], and the fitted in-plane lattice parameters had the same ratio as in the undistorted structure ($\tilde{b}/\tilde{a}=\sqrt{3}$) to within better than 0.02%, so we concluded that the hexagonal symmetry is preserved down to the lowest temperature probed of 2 K.

IV. TRANSITION TO THE HIGH-SYMMETRY STRUCTURE AT HIGH TEMPERATURES

We also measured the diffraction pattern at high temperatures motivated by recent resistivity measurements¹² reporting a weak anomaly near 365 K, proposed to originate from a structural transition. We observed that upon heating the triple-cell peaks decreased in intensity and could not be observed above $T_S=365(3)$ K, which coincides with the location of the transport anomaly. Figure 5(a) shows that triple-cell peaks are absent in the 420 K data and the main structural peaks are only slightly displaced in Q due to lattice expansion. The collected diffraction patterns at various temperatures were refined in the distorted space group $P6_322$, and the obtained temperature dependence of the oxygen displacement ϵ away from the high-symmetry position is plotted in Fig. 5(b) inset and shows a rather rapid decrease near T_S . The lattice parameters increase smoothly with increasing temperature with no clear anomalies near the transition apart from possibly a small kink in the c lattice constant, as linear fits to the data below and above 365 K [solid and dashed lines in Fig. 5(b)] give a slightly smaller slope in the low-temperature phase, consistent with the structural distortion in this phase making the crystal lattice more rigid and so less able to expand upon increasing temperature. The disappearance of the supercell peaks at high temperature indicates a transition to the high-symmetry crystal structure where all Ni-O bonds become equivalent and charge is uniformly distributed on all Ni sites. Indeed, the 420 K data could be well described by the undistorted $P6_3/mmc$ space group with $a_0=2.942\,67(3)$ Å, $c=12.255\,4(2)$ Å and oxygen height $z_{\text{O}}=0.079\,91(6)$ ($R_{\text{Bragg}}=11.8\%$, $R_{\text{F}}=7.13\%$).

To conclude the analysis of the diffraction pattern, we note that in addition to the triple-cell peaks identified above, the data also showed diffraction peaks due to a small admixture (1%) of the rhombohedral $3R$ polytype (currently at the limit at which the pure hexagonal $2H$ polytype can be chemically prepared) and some other small peaks that could not be indexed by any obvious commensurate fractional index of the main peaks and which were still present at high temperatures above the structural transition at 365 K. Those were attributed to unidentified impurity phases below the 1% level that occurred during chemical synthesis [scanning electron microscopy (SEM) coupled with energy-dispersive x-ray analysis (EDX) of a small part of the sample indicated small traces of Au, Al, and Si, but the chemical composition could not be precisely identified]. The alternative origin of those small peaks could have been instrumental (e.g., spurious sample holder reflections).

V. SYMMETRY ANALYSIS OF THE STRUCTURAL DISTORTION

To understand better the mechanism of the structural transition at $T_S=365$ K from the ideal to the distorted structure, we performed an analysis of symmetry-allowed order patterns in the undistorted, high-temperature space group $P6_3/mmc$ with the observed ordering wave vector $\mathbf{q}_0=(1/3, 1/3, 0)$. We considered both the charge (scalar) order

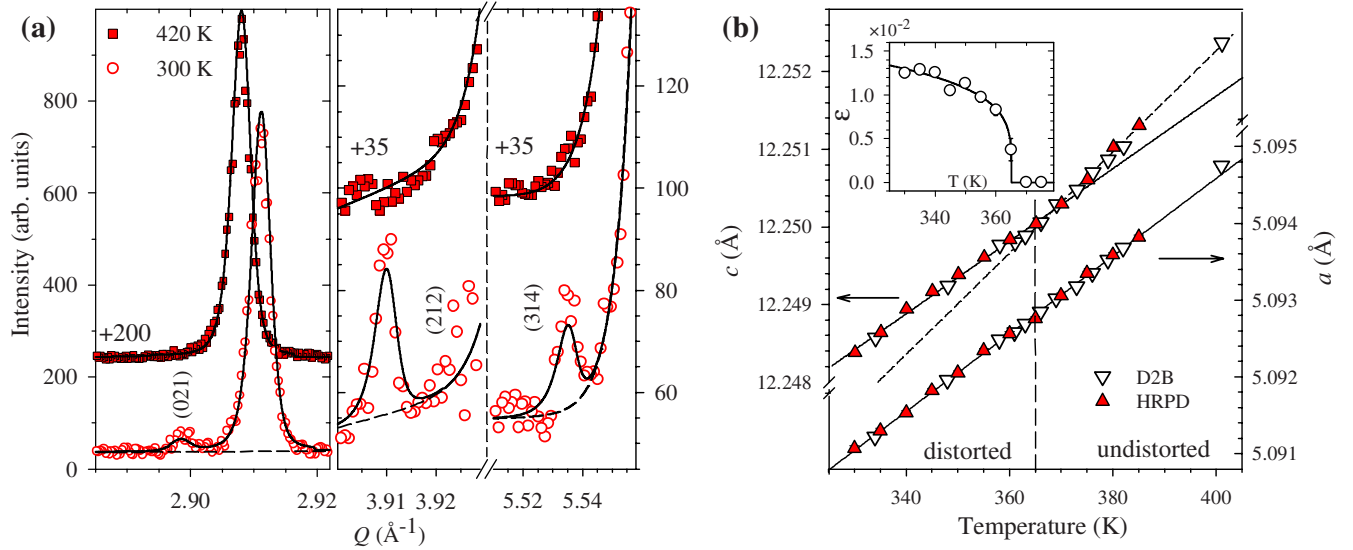


FIG. 5. (Color online) (a) Comparison between 300 K (open symbols, lower trace) and 420 K data (filled symbols, upper trace) showing the absence of the triple-cell peaks (021), (212), and (314) at high temperature. Solid lines are fits to the distorted (300 K) and ideal (420 K) structures, respectively, and dashed lines show the estimated background level. The high-temperature data have been shifted vertically by the indicated offsets for clarity. (b) Temperature dependence of the lattice parameters: c left axis, a right axis. Solid (dashed) lines for the c parameter are straight line fits to the data below (above) $T_S = 365$ K. Filled and open symbols are data from different instruments. Inset: temperature dependence of the oxygen displacement parameter ϵ ; the solid line is a guide to the eye.

on the Ni sites as well as the oxygen ion displacements (polar vector order).

Our refined model for the structure in the distorted phase in Fig. 4 shows a periodic arrangement of expanded (Ni1) $\text{Ni}^{3-\sigma}$ and contracted (Ni2 and Ni3) $\text{Ni}^{3+0.5\sigma}$ sites with $\sigma = 1$ in case of complete charge disproportionation. To try to reproduce this we looked for symmetry-allowed charge (scalar) order patterns with propagation vector $\mathbf{q}_0 = (1/3, 1/3, 0)$ at the Ni $2a$ sites (two atoms) in the unit cell of the $P6_3/mmc$ space group. The obtained irreducible representations and basis vectors are listed in Table II. There are two basis vectors ($\tau_{1,2}$ corresponding to irreducible representations $\Gamma_{1,2}$ in Table II) which physically correspond to having the same or opposite charges for Ni sites above each other in the two layers. The order pattern implied by the structural refinement cannot be described by a single basis vector, but can be described by a linear combination of two basis vectors, i.e.,

$$\zeta = e^{i\pi/3}[(\tau_1 + \tau_2) + e^{i4\pi/3}(\tau_1 - \tau_2)], \quad (1)$$

where $\tau_i(1)$ is the charge on atom 1 (layer 1) for the basis vector τ_i , etc.

TABLE II. Basis vectors for the irreducible representations for charge (scalar) order at the Ni sites ($2a$) in space group $P6_3/mmc$ (no. 194) for propagation vector $\mathbf{q}_0 = (1/3, 1/3, 0)$ obtained using group theory (Ref. 22).

Position	(0,0,0)	(0,0,1/2)
Γ_1	1	1
Γ_2	1	-1

The corresponding charge order pattern (relative to the uniform high-temperature phase where each Ni site has valence +3) is shown in Fig. 6 and consists of a triangular lattice of charges $-\sigma$, i.e., electron-rich $\text{Ni}^{3-\sigma}$, surrounded by a honeycomb network of charges $+0.5\sigma$, i.e., $\text{Ni}^{3+0.5\sigma}$. This charge order pattern is obtained from the basis vector ζ modulated by the phase factor due to the propagation vector \mathbf{q}_0 , i.e., in the unit cell at distance $\mathbf{r} = n_1\mathbf{a}_0 + n_2\mathbf{b}_0 + n_3\mathbf{c}$ from the origin ($n_{1,2,3}$ integers) the charges are given by the real part of the complex vector

$$\tilde{Q}_r = \frac{\sigma}{2} e^{iq_0 r} \zeta. \quad (2)$$

For atom 1 (layer 1) the charge is

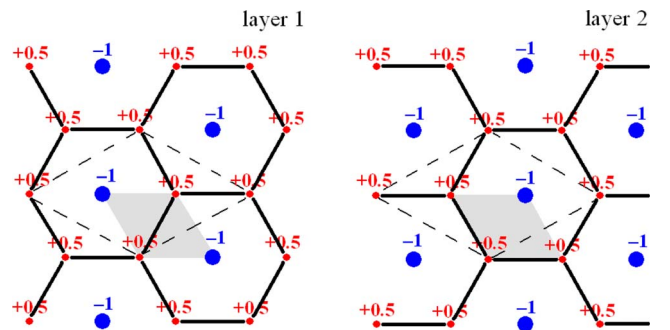


FIG. 6. (Color online) Charge order pattern described by Eq. (2) to be compared with Fig. 4. Labels -1 and $+0.5$ indicate charges in units of σ . Thick hexagonal contours indicate the honeycomb network of the electron-depleted Ni_{2,3} sites and dashed line contour is the unit cell of the charge ordered structure. The light shaded area is the unit cell of the ideal structure with all Ni sites equivalent.

TABLE III. Basis vectors of the irreducible representations for displacement (polar vector) order at the oxygen sites (4*f*) in space group $P6_3/mmc$ (no. 194) for propagation vector $\mathbf{q}_0=(1/3, 1/3, 0)$ obtained using group theory (Ref. 22).

Position	$(2/3, 1/3, z_0)$	$(1/3, 2/3, 1-z_0)$	$(2/3, 1/3, 1/2-z_0)$	$(1/3, 2/3, 1/2+z_0)$
Γ_1	$(e^{i\pi/6}, e^{i\pi/2}, 0)$	$(e^{i\pi/2}, e^{i\pi/6}, 0)$	$(e^{i\pi/6}, e^{i\pi/2}, 0)$	$(e^{i\pi/2}, e^{i\pi/6}, 0)$
Γ_2	$(e^{i\pi/6}, e^{i\pi/2}, 0)$	$(e^{i\pi/2}, e^{i\pi/6}, 0)$	$-(e^{i\pi/6}, e^{i\pi/2}, 0)$	$-(e^{i\pi/2}, e^{i\pi/6}, 0)$

$$Q_r(1) = \sigma \cos(\mathbf{q}_0 \mathbf{r} + \pi/3) \quad (3)$$

and for atom 2 (layer 2) is

$$Q_r(2) = \sigma \cos(\mathbf{q}_0 \mathbf{r} + 5\pi/3). \quad (4)$$

The normalization prefactor in Eq. (2) gives the magnitude of the charge order and was chosen such as to obtain charge $-\sigma$ on the Ni1 sites.

Subsequently we looked at possible order patterns for oxygen ion displacements corresponding to the same propagation wave vector \mathbf{q}_0 . There are in total four one-dimensional and two two-dimensional irreducible representations that could describe displacement (polar vector) order at the 4*f* oxygen sites (four atoms per unit cell) and the two one-dimensional representations relevant for our discussion are listed in Table III. Basis vectors of these representations transform in the same way under the symmetry operations of the $P6_3/mmc$ space group as the basis vectors for charge order listed in Table II so we use the same symbols τ_1 and τ_2 . Here they have complex components indicating a degeneracy with respect to rotation of the displacement vector in the *ab* plane. We again find that the observed structural displacements cannot be described by a single basis vector, but is described by a linear combination of two basis vectors, i.e.,

$$\xi = \frac{1}{2} e^{i7\pi/6} [(\tau_1 + \tau_2) + e^{i4\pi/3} (\tau_1 - \tau_2)], \quad (5)$$

where the complex phase factor in front serves to rotate the oxygen displacement vector in the *ab* plane and with the chosen phase the displacement pattern is as in Fig. 4, i.e., oxygens displaced radially out of the expanded Ni sites (the numerical prefactor is used for normalization). In the above equation $\tau_i(1)$ is the complex displacement vector for atom 1 in the representation τ_i as per Table III. (Note that we use bold symbols to indicate vectors with components along the three crystallographic directions.) The relative phase factor of the τ_1 and τ_2 basis vectors is the same for the polar order of oxygen displacements, Eq. (5), and for the charge order on the Ni sites, Eq. (1), as expected if the structural transition was driven by charge fluctuations coupled to an oxygen phonon breathing mode. It is noteworthy that the obtained oxygen displacements are consistent with an optic phonon mode at the Brillouin zone corner point \mathbf{q}_0 predicted by lattice dynamics calculations²³ for a structure identical to one undistorted NiO₂ layer. So our results provide support for the idea that it is this phonon mode (probably modified slightly due to couplings with the Ag layer above and below) that mediates the $\sqrt{3} \times \sqrt{3}$ charge order in the triangular NiO₂ planes.

In Appendix B we provide further symmetry analysis of the basis vector modes for the charge and displacement orders using corepresentation analysis and prove that they uniquely identify the distorted space group as $P6_322$.

To conclude this section, for completeness we quote below the expressions for obtaining the individual atomic displacements starting from the basis vector mode ξ . The order pattern is given by ξ modulated by the phase factor due to the propagation vector \mathbf{q}_0 , i.e.,

$$\tilde{\mathbf{d}}_r = 2\epsilon e^{i\mathbf{q}_0 \mathbf{r}} \xi, \quad (6)$$

where $\mathbf{r}=(n_1, n_2, n_3)$ defines the unit cell and $\xi(1)$ is the basis vector for atom 1, etc. The scale prefactor 2ϵ was introduced such as to give the absolute magnitude of the final displacements $\epsilon\sqrt{3}a_0$ as per Table I. The real part of the above equation gives the actual displacement vectors

$$2\epsilon(\cos(\mathbf{q}_0 \mathbf{r} + \phi_x), \cos(\mathbf{q}_0 \mathbf{r} + \phi_y), 0), \quad (7)$$

where the phases $\phi_{x,y}$ are given by the basis vector for that atom $\xi=(e^{i\phi_x}, e^{i\phi_y}, 0)$ using Eq. (5) and Table III. For example, for the oxygen atom 1 in the unit cell at the origin $\mathbf{r}=(0, 0, 0)$ the displacement is

$$2\epsilon(\cos(4\pi/3), \cos(5\pi/3), 0) = \epsilon(-1, 1, 0). \quad (8)$$

VI. SUSCEPTIBILITY AND SPECIFIC HEAT

Magnetic susceptibility measured on a small powder sample is shown in Fig. 7(a). The pronounced drop at low temperatures near 20 K (see inset) is attributed to the onset of magnetic order and at higher temperatures above ~ 70 K the data can be well described by a local-moment Curie-Weiss form plus a small temperature-independent part χ_0 ,

$$\chi = \frac{C}{T - \theta} + \chi_0, \quad (9)$$

where $C=0.445(5)$ emu K/mole, $\theta_{CW}=-107(2)$ K, and $\chi_0 = 1.7(1) \times 10^{-4}$ emu/mole, similar to previous reports.¹⁵ The large negative Curie-Weiss temperature shows dominant antiferromagnetic interactions. Magnetic order occurs only at significantly lower temperatures, ~ 20 K, suggesting that fluctuations due to the low dimensionality (mainly in-plane interactions) and the frustrated triangular geometry are important in suppressing the magnetic ordering temperature.

The effective magnetic moment extracted from the Curie-Weiss fit is $\mu_{\text{eff}}=1.88\mu_B$ per Ni ion, and this was used previously¹⁵ as evidence that Ni sites were in the low-spin Ni³⁺ state ($t_{2g}^6 e_g^1$) with $S=1/2$ ($\mu_{\text{eff}}=1.73\mu_B$ for $g=2$). How-

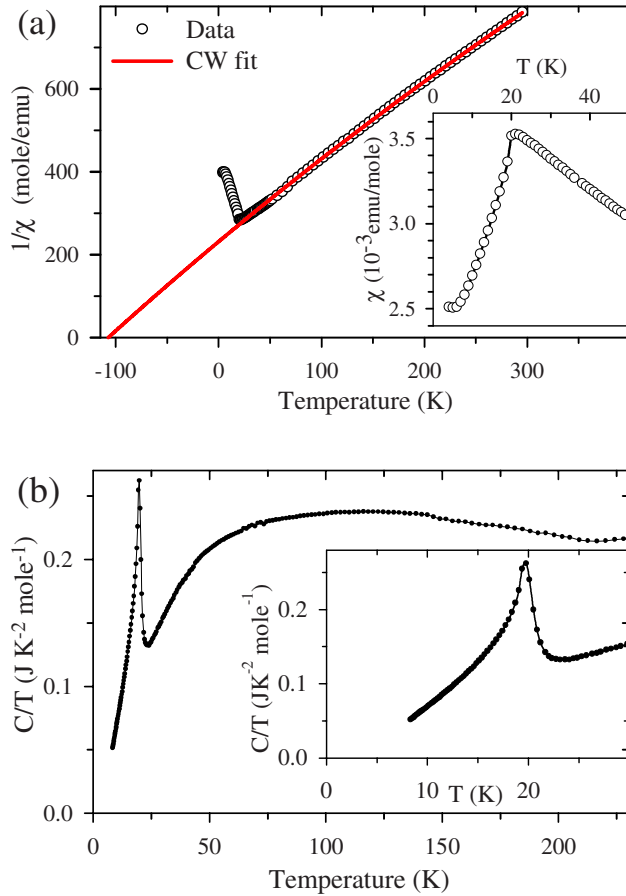


FIG. 7. (Color online) (a) Inverse magnetic susceptibility ($1/\chi$) fitted to a Curie-Weiss law Eq. (1) (solid line) gives a large negative intercept indicating dominant antiferromagnetic interactions. Inset shows suppression of susceptibility below 20 K attributed to onset of antiferromagnetic order. (b) Temperature dependence of the specific heat observing a sharp lambda-like peak near the magnetic transition temperature.

ever, a charge disproportionation scenario as suggested by our structural measurements could also lead to similar values of the effective moment. In the extreme case of complete charge disproportionation the Ni1 site is $\text{Ni}^{2+} t_{2g}^6 e_g^2$ with a large spin moment $S=1$, whereas the other sites are $\text{Ni}^{3.5+}$ likely to have only a very small spin moment as they are close to Ni^{4+} with a filled t_{2g}^6 level, which has $S=0$. The average effective moment observed by high-temperature susceptibility considering only $S=1$ moments on the Ni1 sites would then be $\mu_{\text{eff}}=1.63\mu_B$ (for $g=2$), which is only 6% lower than the value for $S=1/2$ at every site, and it is possible that including a more realistic scenario of partial charge disproportionation (more likely to be the case here) could bring this estimate closer to the experiment.

Finally, we plot in Fig. 7(b) specific heat measurements which observe a sharp lambda-like peak identified with the magnetic transition near 20 K. No other anomalies could be observed up to the highest temperature studied of 240 K, consistent with no additional (structural) transitions occurring in this temperature range.

VII. MAGNETIC STRUCTURE

The magnetic susceptibility shown in Fig. 7(a) inset has a sharp downturn below 20 K which is characteristic of a transition to antiferromagnetic order, and below this temperature additional reflections are observed in the neutron diffraction pattern at low Q . The magnetic order peaks are most easily seen in the difference pattern 4 K–300 K shown in Fig. 8 and can be indexed with respect to the $P6_322$ supercell by the commensurate propagation vector $\mathbf{k}=(1/2,0,0)$. The magnetic order parameter curves are plotted in Fig. 9 as a function of reduced temperature T/T_N . The Néel temperature obtained from the neutron data is 23.7(3) K, slightly higher than the location of the specific heat anomaly near 19.7(3) K, and the susceptibility maximum near 21(1) K. This is probably due to a small temperature calibration offset in the neu-

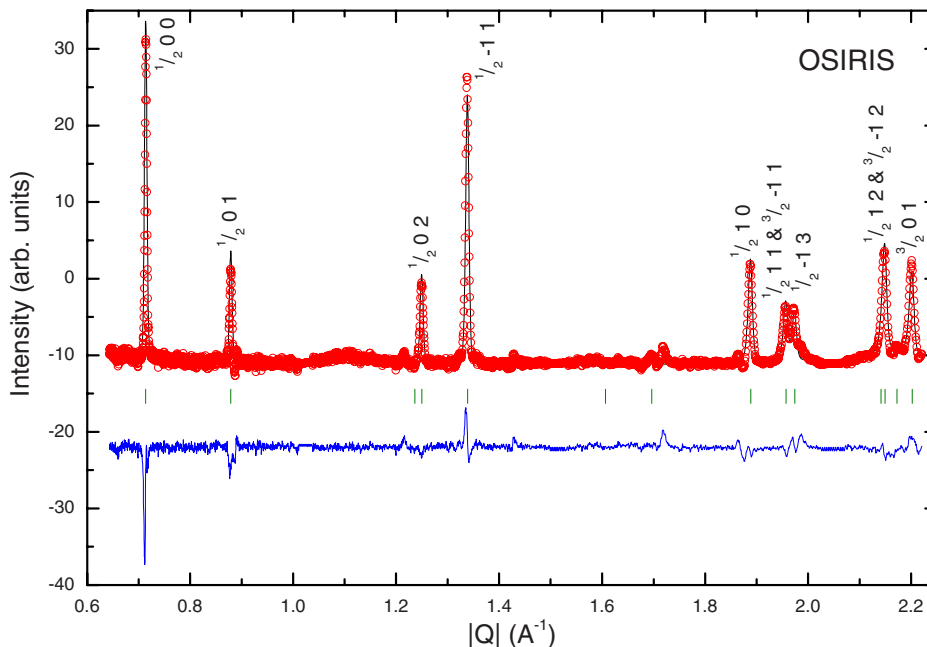


FIG. 8. (Color online) Difference pattern 4 K–300 K from OSIRIS showing peaks of magnetic origin, indexed by the propagation vector $\mathbf{k}=(1/2,0,0)$. The circles represent the observed intensities; the solid curve is a fit to the magnetic structure depicted in Fig. 10 and vertical bars indicate the magnetic Bragg peak positions. The bottom curve shows the difference between the fit and the data.

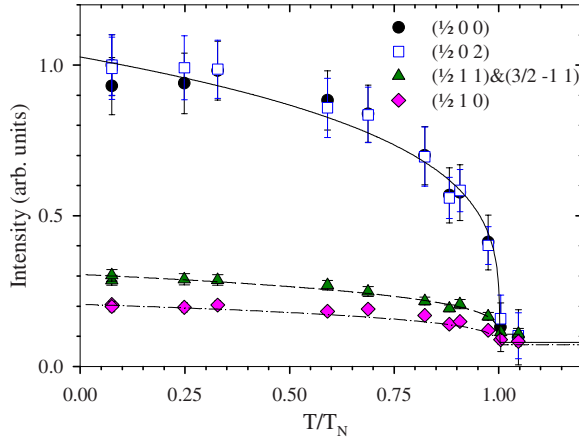


FIG. 9. (Color online) Observed intensity of several magnetic Bragg peaks as a function of reduced temperature T/T_N . Data points are from elastic neutron powder scattering measurements using IN6. Lines are guides to the eye.

tron measurement, where the sensor was at some distance away from the sample. We regard the absolute value of the transition temperature observed by the specific heat measurement $T_N=19.7(3)$ K as the most accurate, in agreement with recent muon spin resonance (μ SR) results.²⁴

To find the magnetic structure we first consider in Table IV the magnetic basis vectors compatible with the symmetry of the $P6_322$ crystal structure for the six Ni ions in the unit cell (three sublattices). Symmetry constrains the moments on the same sublattice to be either parallel or antiparallel between the two layers in the unit cell. The best fit to the observed diffraction pattern (varying the spin direction and magnitude independently on the three sublattices) was obtained for the case when only one of the three sublattices was ordered, either Ni1 or Ni3, with a moment of $1.552(7)\mu_B$ along the c axis and spins parallel between adjacent layers (irreducible representation Λ_3 in Table IV with $v \neq 0$ or $v'' \neq 0$ and all the other spin components equal to 0). This correlates well with the structural analysis whereby the Ni1 site should have a large spin moment ($S=1$ at complete charge disproportionation Ni^{2+}), whereas the other two sites (Ni2 and Ni3) with valences close to $\text{Ni}^{3.5+}$ would have a much smaller moment, as their configuration would be close to Ni^{4+} with $S=0$. Therefore we associate the magnetic order with site Ni1 carrying the largest spin moment.

The experimental data do not preclude the possibility of having also a very small magnetic moment along the c axis

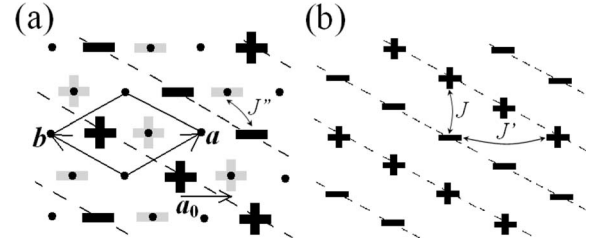


FIG. 10. (a) Magnetic structure of the Ni1 sublattice consisting of alternating rows (dashed lines) of ferromagnetically aligned spins. \pm symbols indicate the projection of the spin moment along the c axis; dots represent the unordered (Ni2 and Ni3) Ni sites in the unit cell (solid contour). Thick black symbols indicate the moments in the bottom NiO_2 plane ($z=1/4$) whereas faint gray symbols correspond to the moments in the upper plane ($z=3/4$) obtained by shifting the pattern by an in-plane offset \mathbf{a}_0 . The arrowed line labeled J'' indicates one of the three interlayer exchange paths. The drawn structure has propagation vector $\mathbf{k}=(1/2,0,0)$ (Bragg peaks indicated by black stars in Fig. 11); equivalent structures are obtained by $\pm 60^\circ$ rotation around the $(2/3, 1/3, z)$ axis. (b) In a single layer the ordered sites form a triangular lattice of spacing a . Short and long arrowed lines indicate the nearest- and next-nearest-neighbor exchanges J and J' in a minimal model proposed to explain the stability of the observed structure.

on either the Ni2 or Ni3 sites; these, however, could only be of the order of $0.1\mu_B$ at maximum (the spin arrangement would then be described by Λ_3 with v' or v'' equal to $-0.1\mu_B$, respectively). Because taking into account these small magnetic moments does not improve the quality of fit, in the following we assume for simplicity that only the sublattice Ni1 is ordered with a large spin moment.

The magnetic structure is illustrated in Fig. 10(a) and consists of alternating ferromagnetic stripes, i.e., spins are parallel along one of the three directions in the triangular plane and antiparallel along the other two directions. This structure can occur in three different domains obtained by $\pm 60^\circ$ rotation around the c axis, which would correspond to the symmetry-equivalent wave vectors $\mathbf{k}'=(0,1/2,0)$ and $\mathbf{k}''(1/2,-1/2,0)$ of the star of \mathbf{k} . We note that the magnetic structure has only a twofold symmetry rotation axis along the c axis, whereas the crystal structure has threefold rotation symmetry along the c axis. Three equal-weighted domains of those three structures would be expected in a macroscopic sample and each domain has the same powder-averaged diffraction pattern.

TABLE IV. Basis vectors for irreducible representations for magnetic order at the six Ni ions in the unit cell (three independent sublattices) for a structure with propagation vector $\mathbf{k}=(1/2,0,0)$ for the $P6_322$ space group obtained using group theory [MODY package (Ref. 22)]. $u, v, u', v', u'',$ and v'' are independent spin components.

Site	Ni1 ($2c$)		Ni2 ($2b$)		Ni3 ($2d$)	
	$(1/3, 2/3, 1/4)$	$(2/3, 1/3, 3/4)$	$(0, 0, 1/4)$	$(0, 0, 3/4)$	$(1/3, 2/3, 3/4)$	$(2/3, 1/3, 1/4)$
Λ_1	$(2u, u, 0)$	$(2u, u, 0)$	$(2u', u', 0)$	$(-2u', -u', 0)$	$(2u'', u'', 0)$	$(2u'', u'', 0)$
Λ_2	$(0, -u, v)$	$(0, -u, -v)$	$(0, -u', v')$	$(0, u', v')$	$(0, -u'', v'')$	$(0, -u'', -v'')$
Λ_3	$(0, -u, v)$	$(0, u, v)$	$(0, -u', v')$	$(0, -u', -v')$	$(0, -u'', v'')$	$(0, u'', v'')$
Λ_4	$(2u, u, 0)$	$(-2u, -u, 0)$	$(2u', u', 0)$	$(2u', u', 0)$	$(2u'', u'', 0)$	$(-2u'', -u'', 0)$

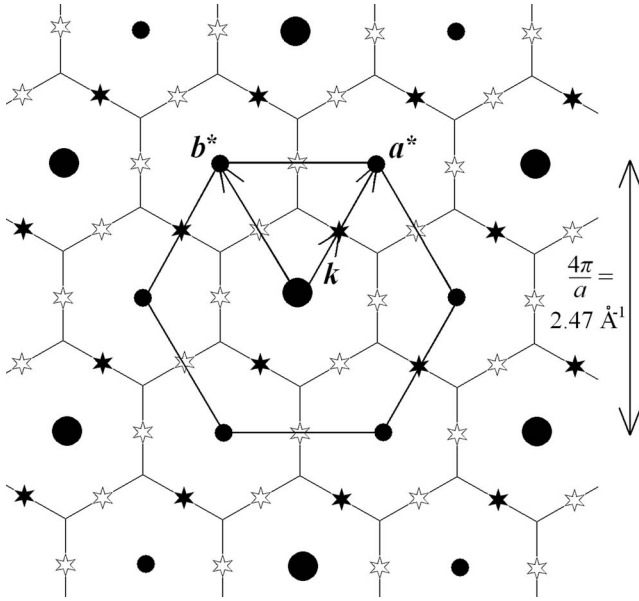


FIG. 11. Reciprocal basal plane showing locations of structural (filled circles) and magnetic reflections (stars). Large filled circles and large bold hexagon indicate the zone centers and Brillouin zone of the ideal, undistorted structure ($P6_3/mmc$), whereas small filled circles and thin line hexagons are, respectively, structural supercell peaks and the Brillouin zone of the distorted crystal structure ($P6_322$). Filled stars are the magnetic Bragg peak positions from the magnetic structure with propagation wave vector $k=(1/2,0,0)$ shown in Fig. 10; open stars are peaks from domains rotated by $\pm 60^\circ$.

In the following we discuss possible mechanisms to stabilize the observed magnetic structure in a model of stacked triangular layers, so we consider the Hamiltonian

$$\mathcal{H} = \sum_{\text{NN}} JS_i \cdot S_j + \sum_{\text{NNN}} J'S_i \cdot S_k + \sum_{\text{interlayer}} J''S_i \cdot S_l - D \sum_i (S_i^z)^2. \quad (10)$$

Here NN indicates summing over all in-plane nearest-neighbor pairs with coupling J , NNN denotes next-nearest-neighbor in-plane pairs with coupling J' [see Fig. 10(b)], and J'' is the interlayer coupling [three neighbors above and three below; see Fig. 10(a)], with $J, J' > 0$ (antiferromagnetic) and $J'' < 0$ (ferromagnetic). The last term in Eq. (10) is an on-site easy-axis anisotropy proposed to arise from crystal-field effects and required to stabilize the ordering spin direction along the crystallographic c axis.

Considering first the 2D antiferromagnetic Heisenberg model [$D=J''=0$ in Eq. (10)] the ground state for NN couplings only is the three-sublattice 120° spiral; however, adding moderate antiferromagnetic NNN couplings $1/8 \leq J'/J \leq 1$ stabilizes the collinear stripe order.²⁵ In fact, for this model at the classical level the two-sublattice stripe order is degenerate with a continuous manifold of four-sublattice noncollinear states, but zero-point quantum fluctuations are predicted to lift this degeneracy through “order by disorder” and select the stripe ground state. An easy-axis anisotropy $D > 0$ is expected to further stabilize the collinear state,

thereby reducing the minimal required J' . At the classical level, in the limit of very large anisotropy approaching the Ising limit, the required J' becomes infinitesimally small, but is nonzero.²⁶ In particular, the NNN couplings are required to lift the degeneracy between the stripe state and the collinear state with two spins up and one down for each triangle, the so-called up-up-down state (UUD), with the ground state energy per spin $e^S = (-J - J')S^2$ lower than $e^{\text{UUD}} = (-J + 3J')S^2$ for antiferromagnetic J' . As an alternative to NNN couplings, we note that the interlayer interactions could also provide a mechanism to lift this degeneracy as the stacking of magnetic layers energetically favors the stripe order. The interlayer energy is $J''S^2$ (energy gain for $J'' < 0$ ferromagnetic) for the stacked stripe order depicted in Fig. 10(a), where each spin has four favorable and two unfavorable interlayer bonds, whereas for a stacked UUD structure the interlayer energy is reduced to $J''S^2/3$ because only 2/3 of the sites have two net favorable bonds and the remaining 1/3 have two net unfavorable interlayer bonds. From this we conclude that the observed magnetic structure could be explained starting from an easy-axis nearest-neighbor triangular antiferromagnet with additional weak in-plane second-neighbor antiferromagnetic exchange or weak ferromagnetic interlayer couplings.

VIII. DISCUSSION AND CONCLUSIONS

To summarize, we have reported high-resolution neutron powder diffraction measurements in the orbitally degenerate frustrated triangular magnet $2H\text{-AgNiO}_2$. We have observed a set of weak structural reflections, undetected in previous x-ray measurements, which indicate a small structural distortion with a tripling of the unit cell in the hexagonal basal plane. We have proposed that this could be explained by a periodic contraction and expansion of NiO_6 octahedra in a three-sublattice structure as a consequence of charge disproportionation on the Ni sites. We have also observed that the triple cell peaks disappear at high temperatures above $T_C = 365$ K, indicating a structural transition to the ideal undistorted structure, where all Ni sites are identical, implying that charge is uniformly distributed on the Ni sites. The low-temperature magnetic diffraction pattern is well explained by a structure of ferromagnetic rows ordered antiferromagnetically, but, interestingly, with ordered moments present only on the electron-rich Ni sites, which as a consequence of charge disproportionation would have the largest spin moment ($S=1$ if Ni^{2+}). The observed magnetic structure on the ordered sites has twofold symmetry compared to the three-fold symmetry of the crystal structure. We have proposed that the magnetic structure could be explained starting from an easy-axis triangular lattice antiferromagnet with additional weak in-plane next-nearest-neighbor antiferromagnetic couplings and/or weak ferromagnetic interlayer interactions. Determination of the relative magnitude of the exchanges and anisotropy terms requires measurements of the spin gap and spin-wave dispersion bandwidth and such measurements are in progress.²⁷

Both the magnetic order and structural distortion observed here are very different from the prevailing theoretical model

for Jahn-Teller-active transition metal ions coupled in a triangular lattice arrangement by near 90° metal-oxygen-metal bonds, which predicts ferrodistorive orbital order and dominant ferromagnetic in-plane interactions,³ as indeed observed experimentally in NaNiO_2 .¹⁰ $2H\text{-AgNiO}_2$ shows a different type of structural modulation which suggests an alternative mechanism of lifting the large degeneracy in the orbital sector by means of charge ordering, leading to nonequivalent Ni sites, some electron rich and others electron depleted. In the ideal, undistorted crystal structure, each Ni site has one electron in the twofold-degenerate e_g orbital and at the structural transition below $T_S=365$ K the lattice separates into two subsystems. From each hexagon of Ni ions one electron jumps to the Ni site in the center to form an orbitally non-degenerate e_g^2 state, and this leaves a surrounding honeycomb network of mainly electronically inactive Ni^{4+} sites but with an extra electron for every two sites (most likely itinerant and therefore distributed with equal probability on every site, a $1/8$ -filled e_g orbital on the honeycomb network). Further experiments, in particular NMR, x-ray absorption (XAFS), or photoelectron spectroscopy (XPS), would be needed to confirm such a scenario and determine quantitatively the extent of the charge disproportionation.

Further studies are also needed to understand better the very different magnetic behavior of the expanded and contracted Ni sites, attributed in the charge order scenario to electron-rich and -depleted sites, respectively. Band structure calculations¹⁶ suggest that as a result of charge order the Ni ions in the center of expanded NiO_6 octahedra become more localized, and then the magnetic order at those sites at low temperatures could be understood in terms of stacked triangular lattices with a large spin moment (valence close to Ni^{2+} with $S=1$), whereas the remaining electron-depleted Ni2 and Ni3 sites located inside contracted NiO_6 octahedra maintain a large itinerant character (due to shorter Ni-O distances and thus stronger orbital overlap with the oxygens); in this scenario the itinerant sites do not show a strong tendency to magnetic order because of insufficiently large density of states at the Fermi level. In fact, the band structure calculations suggested that a small ordered moment of $\sim 0.1\mu_B$ may be induced on the contracted Ni3 sites by the ordering of the large Ni1 moments. We note that recent μSR measurements²⁴ have reported an anomalous temperature dependence of the local static magnetic fields which may be due to small ordered moments on the honeycomb Ni sites with a different temperature dependence compared to the large moments on the Ni1 sublattice.

Another interesting aspect worth looking into is the role of interlayer coupling in stabilizing the magnetic order and structural distortion. It could be investigated by looking at a system in which that coupling could be modified without modifying the intralayer exchange integrals. AgNiO_2 is a rare example of a delafossite having two polymorphs whose synthesis is feasible,³⁰ and therefore the ideal candidate for further studies seems to be the $3R\text{-AgNiO}_2$ polytype. The only difference between the latter and $2H\text{-AgNiO}_2$ is the way the NiO_2 layers are stacked on top of each other.

ACKNOWLEDGMENTS

We would like to thank I. I. Mazin and M. D. Johannes

for collaboration on related work and S. J. Blundell, T. Lancaster, N. Shannon, and R. Moessner for useful discussions. We also thank E. Suard and W. Kockelmann for technical assistance with the experiments at the ILL and ISIS, D. Prabhakaran for help with the SQUID and heat capacity measurements, and the initial stages of sample preparation, and A. El-Turki for performing the SEM-EDX analysis. The research was supported in part by EPSRC U.K. Grants No. EP/C51078X/2 (E.W.) and No. GR/R76714/02 (R.C.), a CASE grant from the EPSRC and ILL (E.M.W.), and the EU program at the ILL. The D2B measurements were supported by EPSRC U.K. Grant No. GR/R88601/02.

APPENDIX A: STRUCTURE FACTORS

Here we list the measured and fitted nuclear (Table V) and magnetic (Table VI) structure factors.

APPENDIX B: COREPRESENTATION ANALYSIS OF THE TRIPLE-CELL CRYSTAL STRUCTURE

Here we look in more detail at the symmetry properties of the experimentally determined supercell modulation and show how the basis vectors for the charge and displacement order patterns can be used to uniquely identify the distorted space group. Specifically, we will find all symmetry operations that leave the order pattern invariant to determine the space group. We follow closely Ref. 28, where the basic concepts of corepresentation analysis as applied to the symmetry reduction for \mathbf{q} -vector modulations at a generic point in the Brillouin zone are explained. We first construct from the irreducible representation (irrep) modes a new set of modes, known as corepresentation (corep) modes, which are invariant upon application of the antiunitary operator KI , where I is the inversion operator (h_{13} in Kovalev notation) and K is the complex conjugation. When combined with their complex conjugates, these modes are centrosymmetric even if the propagation vector is not equivalent to its inverse, as is the case here. In other words, the ‘‘corep little group’’ contains all 24 symmetry operators in $P6_3/mmc$. We can then rewrite both the scalar and the polar vector modulations as linear combinations of corep modes, and directly assess their symmetry. It is important to remember that the coefficients of the corep modes are complex conjugated upon application of an antiunitary operator.

The irrep-corep matrix for space group 194 and propagation vector $\mathbf{q}_0=(1/3, 1/3, 0)$ is listed by Kovalev,²⁹ and, for irreducible representations τ_1 and τ_2 can be summarized as follows.

(1) Each of the two irreps generates exactly one corep, which has the same matrices as the original irrep on the unitary operators. For this reason, we will still use the notation τ_1 and τ_2 to indicate the generated coreps.

(2) For operators $h_1, h_3, h_5, h_7, h_9, h_{11}, Kh_{13}, Kh_{15}, Kh_{17}, Kh_{19}, Kh_{21},$ and Kh_{23} , all coefficients are 1 for both τ_1 and τ_2 .

(3) For operators $h_{16}, h_{18}, h_{14}, h_{22}, h_{24}, h_{20}, Kh_4, Kh_6, Kh_2, Kh_{10}, Kh_{12},$ and Kh_8 , coefficients are 1 for τ_1 and -1 for τ_2 .

The corep modes δ can be obtained from the irrep modes τ as

TABLE V. List of supercell structural peaks associated with the tripling of the unit cell in the basal plane with the observed and calculated unit cell structure factors for the model of expanded and contracted Ni-O bonds shown in Fig. 4. The observed $|F|^2$ is the peak intensity corrected for instrumental resolution effects, divided by the peak multiplicity and normalized per unit cell of the $P6_322$ group. For completeness a selection of the nominal peaks of the ideal structure ($P6_3/mmc$ space group) is also given, and the peak indices are given in both space groups.

Q (\AA^{-1})	(h,k,l) $P6_322$	(h,k,l) $P6_3/mmc$	Observed $ F $ (10^{-14} m)	Calculated $ F $ (10^{-14} m)
Nominal peaks				
1.026	002	002	6.24	6.36
2.052	004	004	7.19	6.76
2.469	110	100	1.14	0.94
2.523	111	101	5.89	5.98
2.675	112	102	5.86	6.12
2.911	113	103	2.79	2.90
3.080	006	006	4.49	4.30
3.212	114	104	5.83	5.92
3.562	115	105	6.40	6.52
3.947	116	106	11.36	11.40
4.105	008	008	5.69	5.43
4.278	300	110	18.07	16.55
4.359	117	107	5.34	5.40
Supercell peaks				
1.425	010	2/3 -1/3 0	0.15	0.16
1.515	011	2/3 -1/3 1	0.24	0.24
1.756	012	2/3 -1/3 2	0.05	0.09
2.097	013	2/3 -1/3 3	0.02	0.02
2.851	020	4/3 -2/3 0	0.31	0.35
2.898	021	4/3 -2/3 1	0.57	0.53
2.936	015	2/3 -1/3 5	0.23	0.23
3.031	022	4/3 -2/3 2	0.14	0.19
3.393	016	2/3 -1/3 6	0.00	0.16
3.514	024	4/3 -2/3 4	0.00	0.15
3.807	211	4/3 1/3 1	0.35	0.22
3.836	025	4/3 -2/3 5	0.53	0.50
3.865	017	2/3 -1/3 7	0.46	0.26
3.910	212	4/3 1/3 2	0.60	0.62
4.074	213	4/3 1/3 3	0.37	0.42
4.105	026	4/3 -2/3 6	0.39	0.35
4.295	214	4/3 1/3 4	0.73	0.66
4.562	215	4/3 1/3 5	0.30	0.26
4.586	027	4/3 -2/3 7	0.49	0.56
4.998	028	4/3 -2/3 8	0.35	0.22
5.166	311	5/3 2/3 1	0.67	0.67
5.209	217	4/3 1/3 7	0.37	0.19
5.242	312	5/3 2/3 2	0.71	0.74
5.366	313	5/3 2/3 3	0.56	0.48
5.535	314	5/3 2/3 4	0.77	0.77
5.575	218	4/3 1/3 8	0.63	0.58
5.703	040	8/3 -4/3 0	0.54	0.60
5.726	041	8/3 -4/3 1	0.89	0.90

TABLE V. (*Continued.*)

Q	(h,k,l)	(h,k,l)	Observed $ F $	Calculated $ F $
5.745	315	5/3 2/3 5	0.56	0.65
5.794	042	8/3 -4/3 2	0.41	0.32
5.821	0 1 11	2/3 -1/3 11	0.22	0.21
5.870	0 2 10	4/3 -2/3 10	0.17	0.12

$$\delta = \frac{1}{2}(\tau + KI\tau). \quad (\text{B1})$$

1. Scalar modes

Since Ni is on the inversion center, and the mode is scalar and real, we have $KI\tau = \tau$, and $\delta = \tau$. We can then rewrite the scalar modulation in Eq. (1) as

$$\zeta = e^{i\pi/3}[(\delta_1 + \delta_2) + e^{i4\pi/3}(\delta_1 - \delta_2)]. \quad (\text{B2})$$

2. Vector modes

Here, site permutation, polar vector inversion, and complex conjugation all come into play, since

$$KI\tau(1) = -\overline{\tau(2)}e^{i4\pi/3},$$

$$KI\tau(3) = -\overline{\tau(4)}e^{i4\pi/3}, \quad (\text{B3})$$

where $\tau(1)$ is the mode on atom 1, etc. The irrep modes are

TABLE VI. List of magnetic Bragg peaks with the observed and calculated unit cell structure factors for the magnetic structure in Fig. 10. The observed $|F|^2$ is the peak intensity corrected for instrumental resolution effects, divided by the peak multiplicity and normalized per unit cell of the $P6_322$ group. For completeness the peak indices are given both in the distorted ($P6_322$) and the ideal ($P6_3/mmc$) crystal structures.

Q (\AA^{-1})	(h,k,l) $P6_322$	(h,k,l) $P6_3/mmc$	Observed $ F $ (10^{-14} m)	Calculated $ F $ (10^{-14} m)
0.714	1/2 0 0	1/6 1/6 0	0.61	0.71
0.879	1/2 0 1	1/6 1/6 1	0.28	0.33
1.236	1/2 -1 0	1/2 0 0	0.00	0.00
1.250	1/2 0 2	1/6 1/6 2	0.37	0.39
1.339	1/2 -1 1	1/2 0 1	0.74	0.72
1.607	1/2 -1 2	1/2 0 2	0.00	0.00
1.697	1/2 0 3	1/6 1/6 3	0.16	0.16
1.889	1/2 1 0	-1/6 5/6 0	0.58	0.63
1.957	1/2 1 1	1/6 5/6 1	0.34	0.35
1.957	3/2 -1 1	1/6 5/6 1	0.34	0.35
1.974	1/2 -1 3	1/2 0 3	0.48	0.45
2.142	3/2 0 0	1/2 -1 0	0.00	0.00
2.150	1/2 1 2	1/6 5/6 2	0.50	0.53
2.150	3/2 -1 2	1/6 5/6 2	0.50	0.53
2.173	1/2 0 4	1/6 1/6 4	0.15	0.20
2.202	3/2 0 1	1/2 -1 1	0.70	0.68

$$\begin{aligned}\boldsymbol{\tau}(1) &= \pm \boldsymbol{\tau}(3) = (e^{i\pi/6}, e^{i\pi/2}, 0), \\ \boldsymbol{\tau}(2) &= \pm \boldsymbol{\tau}(4) = (e^{i\pi/2}, e^{i\pi/6}, 0),\end{aligned}\quad (\text{B4})$$

where the + and – are for irreps 1 and 2, respectively (see $\boldsymbol{\tau}_1$ and $\boldsymbol{\tau}_2$ in Table III). By inserting Eqs. (B3) and (B4) into Eq. (B1), after some manipulation, one obtains

$$\boldsymbol{\delta} = \frac{\sqrt{3}}{2} e^{-i\pi/6} \boldsymbol{\tau}. \quad (\text{B5})$$

We can then rewrite the vector modulation Eq. (5) as

$$\boldsymbol{\xi} = \frac{\sqrt{3}}{3} e^{i4\pi/3} [(\boldsymbol{\delta}_1 + \boldsymbol{\delta}_2) + e^{i4\pi/3} (\boldsymbol{\delta}_1 - \boldsymbol{\delta}_2)]. \quad (\text{B6})$$

3. Symmetry analysis

It is now straightforward to perform the symmetry analysis on the scalar and vector modulation. There are four cases, depending on whether the operators are unitary or antiunitary and whether their matrices have the same or opposite signs for $\boldsymbol{\tau}_1$ and $\boldsymbol{\tau}_2$ or $\boldsymbol{\tau}_1$ and $\boldsymbol{\tau}_2$.

Case 1. Unitary, same sign (e.g., h_3),

$$h_3 \boldsymbol{\zeta} = e^{i\pi/3} [(\boldsymbol{\delta}_1 + \boldsymbol{\delta}_2) + e^{i4\pi/3} (\boldsymbol{\delta}_1 - \boldsymbol{\delta}_2)] = \boldsymbol{\zeta},$$

$$h_3 \boldsymbol{\xi} = \frac{\sqrt{3}}{3} e^{i4\pi/3} [(\boldsymbol{\delta}_1 + \boldsymbol{\delta}_2) + e^{i4\pi/3} (\boldsymbol{\delta}_1 - \boldsymbol{\delta}_2)] = \boldsymbol{\xi} \quad (\text{B7})$$

so both modes are invariant.

Case 2. Unitary, opposite sign (e.g., h_{16}),

$$h_{16} \boldsymbol{\zeta} = e^{i\pi/3} [(\boldsymbol{\delta}_1 - \boldsymbol{\delta}_2) + e^{i4\pi/3} (\boldsymbol{\delta}_1 + \boldsymbol{\delta}_2)] \neq \boldsymbol{\zeta},$$

$$h_{16} \boldsymbol{\xi} = \frac{\sqrt{3}}{3} e^{i4\pi/3} [(\boldsymbol{\delta}_1 - \boldsymbol{\delta}_2) + e^{i4\pi/3} (\boldsymbol{\delta}_1 + \boldsymbol{\delta}_2)] \neq \boldsymbol{\xi}, \quad (\text{B8})$$

so neither mode is invariant.

Case 3. Antiunitary, same sign (e.g., Kh_{13}),

$$Kh_{13} \boldsymbol{\zeta} = e^{-i\pi/3} [(\boldsymbol{\delta}_1 + \boldsymbol{\delta}_2) + e^{-i4\pi/3} (\boldsymbol{\delta}_1 - \boldsymbol{\delta}_2)] \neq \boldsymbol{\zeta},$$

$$Kh_{13} \boldsymbol{\xi} = \frac{\sqrt{3}}{3} e^{-i4\pi/3} [(\boldsymbol{\delta}_1 + \boldsymbol{\delta}_2) + e^{-i4\pi/3} (\boldsymbol{\delta}_1 - \boldsymbol{\delta}_2)] \neq \boldsymbol{\xi}, \quad (\text{B9})$$

so neither mode is invariant.

Case 4. Antiunitary, opposite sign (e.g., Kh_6),

$$\begin{aligned}Kh_6 \boldsymbol{\zeta} &= e^{-i\pi/3} [(\boldsymbol{\delta}_1 - \boldsymbol{\delta}_2) + e^{-i4\pi/3} (\boldsymbol{\delta}_1 + \boldsymbol{\delta}_2)] \\ &= e^{-i5\pi/3} (\boldsymbol{\delta}_1 + \boldsymbol{\delta}_2) + e^{-i\pi/3} (\boldsymbol{\delta}_1 - \boldsymbol{\delta}_2) \\ &= e^{i\pi/3} (\boldsymbol{\delta}_1 + \boldsymbol{\delta}_2) + e^{i5\pi/3} (\boldsymbol{\delta}_1 - \boldsymbol{\delta}_2) = \boldsymbol{\zeta},\end{aligned}$$

$$\begin{aligned}Kh_6 \boldsymbol{\xi} &= \frac{\sqrt{3}}{3} e^{-i4\pi/3} [(\boldsymbol{\delta}_1 - \boldsymbol{\delta}_2) + e^{-i4\pi/3} (\boldsymbol{\delta}_1 + \boldsymbol{\delta}_2)] \\ &= \frac{\sqrt{3}}{3} [e^{-i2\pi/3} (\boldsymbol{\delta}_1 + \boldsymbol{\delta}_2) + e^{-i4\pi/3} (\boldsymbol{\delta}_1 - \boldsymbol{\delta}_2)] \\ &= \frac{\sqrt{3}}{3} [e^{i4\pi/3} (\boldsymbol{\delta}_1 + \boldsymbol{\delta}_2) + e^{i2\pi/3} (\boldsymbol{\delta}_1 - \boldsymbol{\delta}_2)] = \boldsymbol{\xi},\end{aligned}\quad (\text{B10})$$

so both modes are invariant.

In summary, both modes are invariant upon application of the operators h_1 , h_3 , h_5 , h_7 , h_9 , h_{11} , Kh_4 , Kh_6 , Kh_2 , Kh_{10} , Kh_{12} , and Kh_8 and the resulting modulated structure is invariant by the same operators without the complex conjugation. These operators represent all the proper rotations of space group $P6_3/mmc$ —in other words, the sixfold screw axis and the associated orthogonal twofold axes. Taking into account the loss of translational symmetry due to the propagation vector, the resulting space group is $P6_322$ with the unit cell of dimensions $\sqrt{3}a_0 \times \sqrt{3}a_0 \times c$.

¹For a review, see G. Misguich and C. L'Huillier, in *Frustrated Spin Systems*, edited by H. T. Diep (World Scientific, Singapore, 2003), p. 229.

²For a review, see A. Harrison, *J. Phys.: Condens. Matter* **16**, S553 (2004).

³M. V. Mostovoy and D. I. Khomskii, *Phys. Rev. Lett.* **89**, 227203 (2002).

⁴S. Nakatsuji, Y. Nambu, H. Tonomura, O. Sakai, S. Jonas, C. Broholm, H. Tsunetsugu, Y. Qiu, and Y. Maeno, *Science* **309**, 1697 (2005).

⁵F. Vernay, K. Penc, P. Fazekas, and F. Mila, *Phys. Rev. B* **70**, 014428 (2004).

⁶Y. J. Shin, J. P. Doumerc, P. Dordor, C. Delmas, M. Pouchard, and P. Hagenmuller, *J. Solid State Chem.* **107**, 303 (1993).

⁷A. J. W. Reitsma, L. F. Feiner, and A. M. Oleś, *New J. Phys.* **7**, 121 (2005); A.-M. Daré, R. Hayn, and J.-L. Richard, *Europhys. Lett.* **61**, 803 (2003).

⁸J.-H. Chung, Th. Proffen, S. Shamoto, A. M. Ghorayeb, L. Cro-

guennec, W. Tian, B.C. Sales, R. Jin, D. Mandrus, and T. Egami, *Phys. Rev. B* **71**, 064410 (2005), and references therein.

⁹S. J. Clarke, A. J. Fowkes, A. Harrison, R. M. Ibberson, and M. J. Rosseinsky, *Chem. Mater.* **10**, 372 (1998).

¹⁰E. Chappel, M. D. Núñez-Regueiro, G. Chouteau, O. Isnard, and C. Darie, *Eur. Phys. J. B* **17**, 615 (2000); M. Sofin, and M. Jansen, *Z. Naturforsch., B: Chem. Sci.* **60**, 701 (2005), and references therein.

¹¹M. Schreyer and M. Jansen, *Angew. Chem.* **41**, 643 (2002); H. Yoshida, Y. Muraoka, T. Sörgel, M. Jansen, and Z. Hiroi, *Phys. Rev. B* **73**, 020408(R) (2006); J. Sugiyama, Y. Ikeda, K. Mukai, J. H. Brewer, E. J. Ansaldo, G. D. Morris, K. H. Chow, H. Yoshida, and Z. Hiroi, *ibid.* **73**, 224437 (2006); U. Wedig, P. Adler, J. Nuss, H. Modrow, and M. Jansen, *Solid State Sci.* **8**, 753 (2006).

¹²T. Sörgel and M. Jansen, *J. Solid State Chem.* **180**, 8 (2007).

¹³M. D. Johannes, S. Streltsov, I. I. Mazin, and D. I. Khomskii, *Phys. Rev. B* **75**, 180404(R) (2007).

- ¹⁴A. Wichainchai, P. Dordor, J. P. Doumerc, E. Marquestaut, Mi. Pouchard, P. Hagenmuller, and A. Ammar, *J. Solid State Chem.* **74**, 126 (1988).
- ¹⁵T. Sörgel and M. Jansen, *Z. Anorg. Allg. Chem.* **631**, 2970 (2005).
- ¹⁶E. Wawrzyńska, R. Coldea, E. M. Wheeler, I. I. Mazin, M. D. Johannes, T. Sörgel, M. Jansen, R. M. Ibberson, and P. G. Radaelli, *Phys. Rev. Lett.* **99**, 157204 (2007).
- ¹⁷J. Rodriguez-Carvajal, *Physica B* **192**, 55 (1993).
- ¹⁸K. Nakahigashi, Y. Shimomura, and N. Fukuoka, *Acta Crystallogr., Sect. A: Cryst. Phys., Diffr., Theor. Gen. Crystallogr.* **28**, 234 (1972); D. Rodic, V. Spasojevic, V. Kusigerski, R. Tellgren, and H. Rundlof, *Phys. Status Solidi B* **218**, 527 (2000); P. E. Tomaszewski, *Phase Transitions* **38**, 127 (1992).
- ¹⁹J. M. Tarascon, G. Vaughan, Y. Chabre, L. Seguin, M. Anne, P. Strobel, and G. Amatucci, *J. Solid State Chem.* **147**, 410 (1999); A. Hirano, R. Kanno, Y. Kawamoto, Y. Takeda, K. Yamaura, M. Takano, K. Ohyama, M. Ohashi, and Y. Yamaguchi, *Solid State Ionics* **78**, 123 (1995).
- ²⁰I. D. Brown, in *Structure and Bonding in Crystals*, edited by M. O'Keefe and A. Navrotsky (Academic Press, New York, 1981), Vol. 2, pp. 1–30; N. E. Brese *et al.*, *Acta Crystallogr., Sect. B: Struct. Sci.* **47**, 192 (1991).
- ²¹J. A. Alonso, J. L. García-Muñoz, M. T. Fernández-Díaz, M. A. G. Aranda, M. J. Martínez-Lope, and M. T. Casais, *Phys. Rev. Lett.* **82**, 3871 (1999).
- ²²W. Sikora, F. Białas, and L. Pytlik, *J. Appl. Crystallogr.* **37**, 1015 (2004).
- ²³M. Bejas, A. Greco, and A. Foussats, *Phys. Rev. B* **75**, 033101 (2007).
- ²⁴T. Lancaster, S. J. Blundell, P. J. Baker, M. L. Brooks, W. Hayes, F. L. Pratt, R. Coldea, T. Sörgel, and M. Jansen, *Phys. Rev. Lett.* **100**, 017206 (2008).
- ²⁵A. V. Chubukov and Th. Jolicoeur, *Phys. Rev. B* **46**, 11137 (1992); Th. Jolicoeur, E. Dagotto, E. Gagliano, and S. Bacci, *ibid.* **42**, 4800 (1990).
- ²⁶P. A. Slotte and P. C. Hemmer, *J. Phys. C* **17**, 4645 (1984).
- ²⁷E. M. Wheeler *et al.* (unpublished).
- ²⁸P. G. Radaelli and L. C. Chapon, *Phys. Rev. B* **76**, 054428 (2007).
- ²⁹O. V. Kovalev, in *Irreducible Representations, Induced Representations and Corepresentations*, 2nd ed., edited by H. T. Stokes and D. M. Hatch (Gordon and Breach Science Publishers, New York, 1993), p. 251.
- ³⁰X. X. Liu, C. P. M. Oberndorfer, and M. Jansen, *J. Electrochem. Soc.* **155**, E1 (2008).